



# Structural and thermodynamic limits of layer thickness in 2D halide perovskites

Chan Myae Myae Soe<sup>a,b,1</sup>, G. P. Nagabhushana<sup>c,d,1</sup>, Radha Shivaramaiah<sup>c,d,1</sup>, Hsinhan Tsai<sup>e</sup>, Wanyi Nie<sup>e</sup>, Jean-Christophe Blancon<sup>e</sup>, Ferdinand Melkonyan<sup>a,b</sup>, Duyen H. Cao<sup>a,b</sup>, Boubacar Traoré<sup>f</sup>, Laurent Pedesseau<sup>g</sup>, Mikaël Kepenekian<sup>f</sup>, Claudine Katan<sup>f</sup>, Jacky Even<sup>g</sup>, Tobin J. Marks<sup>a,b</sup>, Alexandra Navrotsky<sup>c,d,2</sup>, Aditya D. Mohite<sup>e,2,3</sup>, Constantinos C. Stoumpos<sup>a,b,2,4</sup>, and Mercouri G. Kanatzidis<sup>a,b,2</sup>

<sup>a</sup>Department of Chemistry, Northwestern University, Evanston, IL 60208; <sup>b</sup>Argonne–Northwestern Solar Energy Research Center, Northwestern University, Evanston, IL 60208; <sup>c</sup>Peter A. Rock Thermochemistry Laboratory, University of California, Davis, CA 95616; <sup>d</sup>Nanomaterials in the Environment, Agriculture, and Technology Organized Research Unit, University of California, Davis, CA 95616; <sup>e</sup>Material Synthesis and Integrated Devices, MPA-11, Los Alamos National Laboratory, Los Alamos, NM 87545; <sup>f</sup>Université de Rennes, École Nationale Supérieure de Chimie de Rennes, Institut National des Sciences Appliquées Rennes, CNRS, Institut des Sciences Chimiques de Rennes–UMR 6226, F-35000 Rennes, France; and <sup>g</sup>Université de Rennes, Institut National des Sciences Appliquées Rennes, CNRS, Institut des Fonctions Optiques pour les Technologies de l'Information–UMR 6082, F-35000 Rennes, France

Contributed by Alexandra Navrotsky, November 7, 2018 (sent for review July 2, 2018; reviewed by Anthony K. Cheetham and James R. Neilson)

In the fast-evolving field of halide perovskite semiconductors, the 2D perovskites  $(A')_2(A)_{n-1}M_nX_{3n+1}$  [where  $A = Cs^+$ ,  $CH_3NH_3^+$ ,  $HC(NH_2)_2^+$ ;  $A'$  = ammonium cation acting as spacer;  $M = Ge^{2+}$ ,  $Sn^{2+}$ ,  $Pb^{2+}$ ; and  $X = Cl^-$ ,  $Br^-$ ,  $I^-$ ] have recently made a critical entry. The  $n$  value defines the thickness of the 2D layers, which controls the optical and electronic properties. The 2D perovskites have demonstrated preliminary optoelectronic device lifetime superior to their 3D counterparts. They have also attracted fundamental interest as solution-processed quantum wells with structural and physical properties tunable via chemical composition, notably by the  $n$  value defining the perovskite layer thickness. The higher members ( $n > 5$ ) have not been documented, and there are important scientific questions underlying fundamental limits for  $n$ . To develop and utilize these materials in technology, it is imperative to understand their thermodynamic stability, fundamental synthetic limitations, and the derived structure–function relationships. We report the effective synthesis of the highest iodide  $n$ -members yet, namely  $(CH_3(CH_2)_2NH_3)_2(CH_3NH_3)_5Pb_6I_{19}$  ( $n = 6$ ) and  $(CH_3(CH_2)_2NH_3)_2(CH_3NH_3)_6Pb_7I_{22}$  ( $n = 7$ ), and confirm the crystal structure with single-crystal X-ray diffraction, and provide indirect evidence for “ $(CH_3(CH_2)_2NH_3)_2(CH_3NH_3)_8Pb_9I_{28}$ ” (“ $n = 9$ ”). Direct HCl solution calorimetric measurements show the compounds with  $n > 7$  have unfavorable enthalpies of formation ( $\Delta H_f$ ), suggesting the formation of higher homologs to be challenging. Finally, we report preliminary  $n$ -dependent solar cell efficiency in the range of 9–12.6% in these higher  $n$ -members, highlighting the strong promise of these materials for high-performance devices.

layered compounds | homologous series | Ruddlesden–Popper halide perovskites | formation enthalpy | photovoltaics

The 2D metal halide perovskites have become highly promising semiconductors with a high degree of structural flexibility and tunable optoelectronic properties (1–18). They have a general formula of  $(A')_2(A)_{n-1}M_nX_{3n+1}$ , where  $A = Cs^+$ ,  $CH_3NH_3^+$  (MA),  $HC(NH_2)_2^+$  (FA),  $M = Ge^{2+}$ ,  $Sn^{2+}$ ,  $Pb^{2+}$ , and  $X = Cl^-$ ,  $Br^-$ ,  $I^-$ , are the perovskite components and  $A'^+$  =  $RNH_3$  is an organic spacer, such as  $CH_3(CH_2)_3NH_3^+$  (BA). Generally, 2D perovskites form from solution via the bottom-up self-assembly of individual, semiconducting perovskite sheets having an adjustable slab thickness of up to few nanometers, separated by insulating bulky organic molecules. As a result, they behave as natural multiple quantum wells (QWs) with the semiconducting perovskite layers representing the wells and the insulating organic spacers representing the barriers. The width of the barrier is fixed and depends only on the length of the  $A'$  cation, while the width of the well can be adjusted by varying the thickness of perovskite slabs, which is defined by the  $n$  variable in  $(A')_2(A)_{n-1}M_nX_{3n+1}$ .

To date, most of the known 2D halide perovskites [so-called Ruddlesden–Popper (RP)] compounds are the early members of

the potentially vast homologous series with most representation coming from  $n = 1$  and  $n = 2$ , while  $n = 3$  and 4 members remain much less explored (1, 3, 5, 7, 10, 15, 19–25). Given the increase in challenges associated with isolation of pure phases and characterization of higher members with thicker slabs, our recently reported  $n = 5$  represents the only structurally characterized example (1, 26), and here we proceed with our investigation of  $n > 5$  members with a twofold objective.

First, it is critical to understand the thermodynamic and chemical limitations of the maximum RP thickness that can be sandwiched between the organic bilayers while retaining the structural integrity of the 2D RP perovskite. Second, the thicker inorganic slabs will present QWs with increased Coulombic

## Significance

Organic–inorganic hybrid perovskites are exciting new solar cell materials. In 2D perovskites, the 3D structure is spatially interrupted by a layer of intercalated ions, which may alter both stability and functionality. A major question concerns the limit to which the 2D architecture can be maintained as the thickness of the layers increases. A combination of synthetic chemistry, crystallography, and spectroscopy was used to obtain and identify the thickest 2D halide perovskite characterized to date, having seven layers. Experimentally measured enthalpies of formation as a function of layer thickness show systematic behavior and that higher homologues are energetically unstable, placing a limit on the number of layers possible in a single-phase 2D perovskite. Their application in photovoltaics is discussed.

Author contributions: C.M.M.S. and M.G.K. designed research; C.M.M.S., G.P.N., R.S., F.M., D.H.C., and C.C.S. performed research; H.T., W.N., J.-C.B., T.J.M., and A.D.M. contributed new reagents/analytic tools; C.M.M.S., R.S., F.M., D.H.C., B.T., L.P., M.K., C.K., J.E., and C.C.S. analyzed data; C.M.M.S., G.P.N., A.N., C.C.S., and M.G.K. wrote the paper; C.M.M.S., H.T., W.N., and J.-C.B. fabricated and characterized thin films; B.T., L.P., and M.K. performed DFT calculations; C.K. and J.E. supervised DFT calculations; T.J.M. supervised synthesis and characterization; A.N. consulted; A.D.M. supervised fabrication and characterization of thin films; C.C.S. and M.G.K. supervised the project.

Reviewers: A.K.C., University of Cambridge; and J.R.N., Colorado State University.

The authors declare no conflict of interest.

Published under the PNAS license.

<sup>1</sup>C.M.M.S., G.P.N., and R.S. contributed equally to this work.

<sup>2</sup>To whom correspondence should be addressed. Email: m-kanatzidis@northwestern.edu, cstoumpos@materials.uoc.gr, aditya.d.mohite@rice.edu, or anavrotsky@ucdavis.edu.

<sup>3</sup>Present address: Department of Chemical and Biomolecular Engineering, Rice University, Houston, TX 77005.

<sup>4</sup>Present address: Department of Materials Science and Technology, University of Crete, Heraklion GR-70013, Greece.

This article contains supporting information online at [www.pnas.org/lookup/suppl/doi:10.1073/pnas.1811006115/-DCSupplemental](http://www.pnas.org/lookup/suppl/doi:10.1073/pnas.1811006115/-DCSupplemental).

shielding, lowering the exciton binding energy and increasing the effective charge carrier mobility (9, 20, 27–31). Therefore, in the higher- $n$  compounds, the excitons will dissociate more efficiently, a desired property for light harvesting in solar cells. As  $n$  increases, the associated optical, electronic, and electrical properties are also expected to further diverge from those of the pure excitonic compounds,  $n = 1, 2$ , and draw closer to those of the end-member,  $n = \infty$ , 3D compounds,  $\text{AMX}_3$ . We hypothesize that the higher  $n$ -value materials are either thermodynamically unstable with respect to simpler members or kinetically cumbersome. The purpose of this work is to address this issue and provide a broader understanding of the stability limits of slab thickness as expressed by the value of  $n$  (slab thickness).

Here, we report the successful synthesis of the highest  $n$ -members yet, namely  $n = 6$  and  $n = 7$ , and confirm the crystal structure using single crystal X-ray diffraction analysis. The increased difficulty in growing phase-pure higher  $n$ -member compounds is supported on thermodynamic grounds as our calorimetric measurements show that the compounds with  $n > 7$  have an unfavorable enthalpy of formation ( $\Delta H_f$ ) with respect to binary compounds and also  $\text{MAPbI}_3$ . As the ability of X-ray diffraction to distinguish between the high  $n$ -members diminishes for increasing  $n$ -members, we use proton NMR ( $^1\text{H-NMR}$ ) as a complementary analysis to quantify the relative ratio between BA and MA based on the chemical formula. After unambiguously establishing the identity of the compounds, we proceed to extend the structure-bandgap map

of RP perovskites ( $E_g = 1.78$  eV and  $E_g = 1.74$  eV for  $n = 6$  and  $n = 7$ , respectively, which are ideal bandgaps for Si/perovskite tandem solar cells). As a demonstration of the potential of these materials for high-efficiency devices, we show that when incorporated into a planar solar cell device structure, the higher  $n$ -members give optimized power conversion efficiencies (PCEs) of 10.9% and 8.93% for  $n = 6$  and  $n = 7$ , respectively.

## Results and Discussion

### Materials Synthesis, Characterization, and Thermodynamic Stability.

The synthetic procedure of the  $n = 6$  and  $n = 7$  iodide compounds is a modified version of our previously reported off-stoichiometry method which is highly important for the synthesis of phase-pure 2D compounds (2). The method becomes even more critical for  $n > 5$  due to the increasingly smaller difference in the weighed amounts of methyl ammonium chloride,  $\text{MACl}$ , and BA incorporated into the acid solution during the synthesis, in going from  $n = 5$  to  $n = 6$  and  $n = 7$ . This implies that the success of the high- $n$ -member synthesis is subject to much more experimental irreproducibility. In addition, as we discuss below, the minimal formation energy difference for the higher  $n$  2D perovskites also introduces a large synthetic uncertainty arising from a smaller thermodynamic driving force to make any specific compound. Nevertheless, the obtained solids still consist of high- $n$  2D iodide perovskites as a major phase, as evidenced by our ability to isolate single crystals of the  $n = 6$  and  $n = 7$  phases. The clear presence

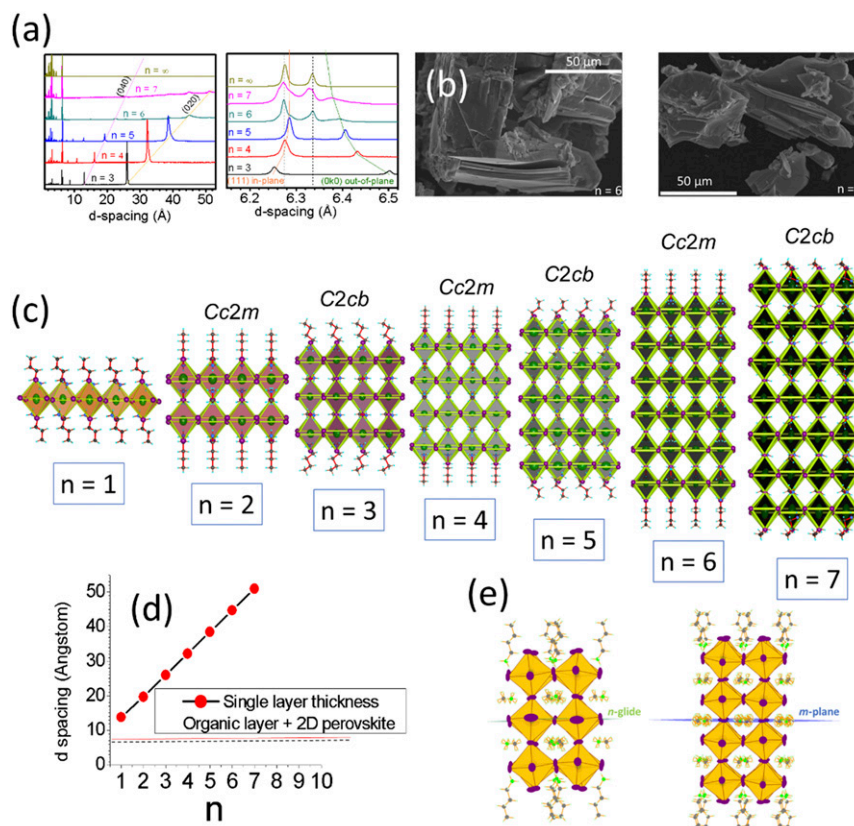


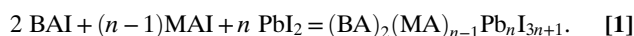
**Fig. 1.** Crystal structure of 2D RP  $(\text{BA})_2(\text{MA})_{n-1}\text{Pb}_n\text{I}_{3n+1}$  ( $n = 1-7$ ). (A) High-resolution synchrotron X-ray patterns presenting the evolution of the diffraction within the  $(\text{BA})_2\text{MA}_{n-1}\text{Pb}_n\text{I}_{3n+1}$  series ( $n = 3-7$ , and 3D) as a function of  $n$ . The solid traces are guides for the eye, while the dashed lines indicate the peak position of the  $n \rightarrow \infty$  3D perovskite. (B) SEM images of the  $n = 6$  and  $n = 7$  members revealing the sheet-like morphology of the crystals, indicative of the 2D nature of the compounds. (C) Crystal structures of the  $(\text{BA})_2(\text{MA})_{n-1}\text{Pb}_n\text{I}_{3n+1}$  RP perovskites at room temperature. Single-layer views for the  $n = 1-7$  RP perovskites viewed along the projection to the  $a$  axis ( $n = 2, 4, 6$ ) and  $c$  axis ( $n = 1, 3, 5, 7$ ). (D) Variation of the  $d$  spacing, capturing the thickness of 1 formula unit, as a function of  $n$ . The thickness of a single octahedron (green dashed line) and the thickness of the organic bilayer (solid purple line) are shown for reference. (E) Odd-numbered layers are characterized by a glide plane passing through the middle layer, whereas the even-numbered layers are related to one another through a mirror plane passing between the two central perovskite layers.

of  $n = 6$  and  $7$  in the X-ray powder diffraction patterns and the plate-like morphology of the crystals in scanning electron microscopy (SEM) images (Fig. 1A and B), along with a series of spectroscopic evidence (SI Appendix, Figs. S1 and S2), all confirm the existence of high- $n$  2D perovskites. The crystal structures of the higher number RP perovskites were determined by single-crystal X-ray diffraction for  $n = 6$  and  $n = 7$  (Figs. 1C and 2A and B and SI Appendix, Fig. S3 and Tables S1–S9). The new members of  $(\text{BA})_2(\text{MA})_{n-1}\text{Pb}_n\text{I}_{3n+1}$  continue the structural motif of the lower  $n$ -members, which shows that layers with odd ( $n = 1, 3, 5, 7, \dots$ ) and even ( $n = 2, 4, 6, 8, \dots$ ) numbers adopt two distinct space groups (Fig. 1C).  $(\text{BA})_2(\text{MA})_5\text{Pb}_6\text{I}_{19}$  ( $n = 6$ ) crystallizes in orthorhombic space group  $Cc2m$ , whereas  $(\text{BA})_2(\text{MA})_6\text{Pb}_7\text{I}_{22}$  crystallizes in the orthorhombic space group  $C2cb$  with each unit cell incorporating two individual layers. The interlayer spacing as reflected in the  $b$  axis as a function of  $n$  value changes in a highly systematic way with  $n$  as shown in Fig. 1D. The major difference between the odd- and even-numbered perovskites lies in the intrinsic symmetry of the layers. Odd-numbered perovskites possess a pseudo-inversion symmetry with a glide plane passing through the middle of the layer; even-numbered perovskites, on the other hand, possess no inversion symmetry, and the layers are related to each other through a mirror plane, which bisects each layer (Fig. 1E).

From the synchrotron X-ray diffraction (SXRD) patterns, the  $n$  value can be determined from the number of characteristic  $(0k0)$  basal peaks below the characteristic  $(111)$  Bragg reflection. The latter arises from the  $\text{Pb} \cdots \text{Pb}$  diffraction planes corresponding to the intralayer diffraction (spacing  $d \sim 6.3 \text{ \AA}$ ) (see full unit cell structure in Figs. 1A and 2A). As the perovskite layer gets thicker (higher  $n$ ), however, the diffraction intensity of the  $0k0$  basal reflections weakens significantly even in intense SXRD data (Fig. 1A). These results are consistent across different batches. Unlike the  $n = 1$ – $5$  members where the experimental patterns exactly correspond to the theoretical ones indicating single-phase samples, for  $n = 6$  and  $7$ , additional XRD peaks can be observed, originating from some 3D  $n = \infty$  phase. When targeting

$n = 6$ , the minor  $n = \infty$  and other lower RP phases such as  $n = 2$  coexist. For  $n = 7$ , on the other hand, small amounts of  $n = 5$  and  $n = 6$  cocrystallize, without any lower number phases. We rationalize this trend by invoking the thermodynamic stability trends of the higher  $n$ -members, which becomes unfavorable by comparison with  $\text{MAPbI}_3$  for  $n > 6$ , as discussed in detail based on the calorimetry data below. The universal plate-like crystal morphology is evident in the SEM images shown in Fig. 1B.

The SXRD and NMR results (see SI Appendix, Fig. S4, and corresponding discussion in SI Appendix) imply that the synthesis of layered perovskites with very large slab thickness ( $n > 5$ ) is challenging under the present self-assembly reaction conditions. To understand why, we measured the enthalpy of formation,  $\Delta H$ , of the series as a function of  $n$  using isothermal solution calorimetry (32). The thermochemical cycle used to calculate the formation enthalpy is given in Table 1. Enthalpies of solution of all of the samples and the components used in the thermochemical cycle are listed in SI Appendix, Table S10. The resulting formation enthalpies from binary iodide components ( $\Delta H_f$ ) are listed in the last column of Table 2, together with some relevant structural and spectroscopic quantities of the 2D perovskites. The formation reaction is given by the following:



The  $\Delta H$  values are negative for low- $n$  compounds ( $n = 1$ – $5$ ) but positive for the compounds with larger  $n$ ; and the observed trend also depends on the odd/even nature of the perovskite layers (Fig. 2C). For compounds with an even number of layers,  $n = 2$  and  $4$ , the formation enthalpy is strongly exothermic and becomes more so with increasing  $n$  ( $n = 4$ ,  $|\Delta H| = -80.6 \pm 3.1 \text{ kJ/mol}$ , and  $n = 2$ ,  $\Delta H = -67.9 \pm 1.5 \text{ kJ/mol}$ ). The formation enthalpies for the compounds with an odd number of layers,  $n = 1, 3$ , and  $5$ , are significantly less exothermic than those for  $n = 2$  and  $4$ . Furthermore, the trend for the compounds with an odd number of layers also seems to be opposite where the formation enthalpy becomes less exothermic with increasing  $n$  ( $n = 1$ ,

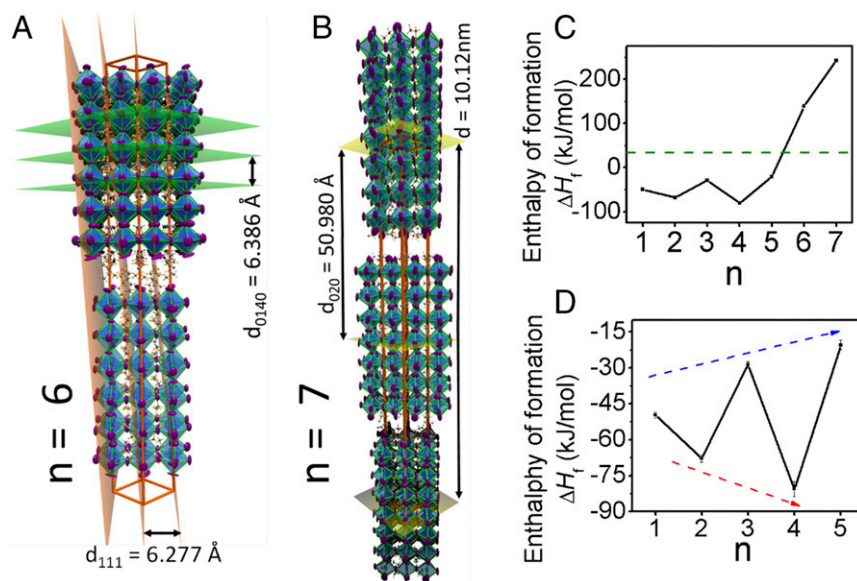


**Fig. 2.** Crystal structure versus thermodynamic stability in 2D RP  $(\text{BA})_2(\text{MA})_{n-1}\text{Pb}_n\text{I}_{3n+1}$ . (A and B) The unit cells of  $n = 6$  (Left) and  $n = 7$  (Right) members of  $(\text{BA})_2(\text{MA})_{n-1}\text{Pb}_n\text{I}_{3n+1}$  incorporating two offset layers. The highlighted planes indicate the most prominent diffraction planes, which correspond to the in-plane  $(111)$  and out-of-plane  $(0k0)$   $\text{Pb}$ – $\text{Pb}$  directions, shown for  $n = 6$ , and the longest  $\text{Pb} \cdots \text{Pb}$  separation  $(020)$  corresponding to the layer width shown for  $n = 7$ . (C) Enthalpy of formation of the  $(\text{BA})_2(\text{MA})_{n-1}\text{Pb}_n\text{I}_{3n+1}$  series as a function of the perovskite layer thickness ( $n$ ), showing the trend with  $n$ . A further difference emerges for even and odd values of  $n$  with a dramatic surge to less stable enthalpy for  $n = 6$  and  $n = 7$ . The dashed line denotes the enthalpy of formation for the  $\text{MAPbI}_3$  3D perovskite (32). (D) An expanded view of the  $n = 1$ – $5$  perovskites, where the odd/even effect is most prominent.

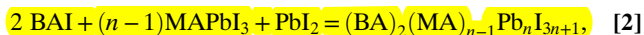
**Table 1. Thermochemical cycle used to calculate the enthalpy of formation of 2D layered (BA)<sub>2</sub>(MA)<sub>n-1</sub>Pb<sub>n</sub>I<sub>3n+1</sub> perovskites (n = 1–7)**

Reaction scheme*	Enthalpy measurement
(BA) <sub>2</sub> (MA) <sub>n-1</sub> Pb <sub>n</sub> I <sub>3n+1</sub> (s) → nPbI <sub>2</sub> (aq) + 2BAI <sub>(aq)</sub> + (n-1)MAI <sub>(aq)</sub>	ΔH <sub>1</sub>
2BAI <sub>(s)</sub> → 2BAI <sub>(aq)</sub>	ΔH <sub>2</sub>
nPbI <sub>2</sub> (s) → nPbI <sub>2</sub> (aq)	ΔH <sub>3</sub>
(n-1)MAI <sub>(s)</sub> → (n-1)MAI <sub>(aq)</sub>	ΔH <sub>4</sub>
nPbI <sub>2</sub> (s) + 2BAI <sub>(s)</sub> + (n-1)MAI <sub>(s)</sub> → BA <sub>2</sub> (MA) <sub>n</sub> -1Pb <sub>n</sub> I <sub>3n+1</sub> (s)	ΔH <sub>f</sub>

$$\Delta H_f = -\Delta H_1 + \Delta H_2 + \Delta H_3 + \Delta H_4.$$

\* (CH<sub>3</sub>(CH<sub>2</sub>)<sub>3</sub>NH<sub>2</sub>)<sub>2</sub> = BA; (CH<sub>3</sub>NH<sub>2</sub>) = MA.

ΔH = -49.7 ± 1.2 kJ/mol; n = 3, ΔH = -28.7 ± 1.3 kJ/mol; and n = 5, ΔH = -20.5 ± 2.1 kJ/mol). Assuming that the entropy of formation (ΔS) in the system decreases slightly or is close to zero as the precursors come together to form a well-defined QW structure, the -TΔS term will be positive, and for a favorable reaction, the ΔH must be negative to obtain negative ΔG. Thus, for the lower-n compounds (n = 1–5) where all of the ΔH values are significantly negative, the Gibbs free energy of formation is almost certainly negative, indicating that these compounds are thermodynamically stable, which is consistent with our experimental findings that these compounds can be synthesized as pure phases from a stoichiometric mixture of components. Going above n = 5, there is a dramatic change toward less exothermic formation enthalpy, going from negative values to positive (Fig. 2 C and D). The enthalpy of formation, ΔH<sub>f</sub>, increases with n, yielding 138.6 ± 1.5 kJ/mol for n = 6 and 242.1 ± 2.0 kJ/mol for n = 7. These values are more positive than for the 3D MAPbI<sub>3</sub> (34.5 ± 1.0 kJ/mol) (32), which does not contain BA. Indeed, one can calculate the enthalpy of the reaction from BAI and MAPbI<sub>3</sub> given by the following:



from the data in *SI Appendix*, Table S10. For n < 6, the values are strongly negative but they are -68.4 kJ/mol for n = 6 and 0.6 kJ/mol for n = 7. This suggests that, for n > 7, the RP phases are thermodynamically unstable, both with respect to binary components and with respect to the 3D perovskite. Thus, there is sharp destabilization in the Gibbs free energy (ΔG) with increasing n, which limits the possibility of product formation. This provides a fundamental thermodynamic explanation of why the systems with n = 6, 7, and larger n values may not be synthesizable in pure form.

To further examine our hypothesis derived from the thermal calorimetry experiments, we attempted to synthesize compounds

with n > 7. The targeted compound, (BA)<sub>2</sub>(MA)<sub>8</sub>Pb<sub>9</sub>I<sub>28</sub>, denoted as “n = 9” based on the stoichiometry of the precursors, did not seem to form in pure form as indicated by the characterization methods compiled in *SI Appendix*, Fig. S5. The powder X-ray diffraction pattern obtained is very similar to 3D MAPbI<sub>3</sub>, but when characterized with NMR, the BA:MA ratio was found to be 1:33 (rather than 1:4), denoting a small BA content in the compound. These analyses could indicate that the “n = 9” sample may be a mixture of MAPbI<sub>3</sub> with a higher-n RP phase(s). However, the alternative possibility of 2D sheets intergrown, either randomly or coherently, within a 3D matrix, is also possible and even likely as this is supported by spectroscopic evidence, which consistently shows a small but persistent blue shift of the bandgap relative to the pure 3D compound. This provides evidence that, in contrast to the claims in several reports (15, 19), stoichiometric synthesis reactions of targeted compounds with n > 7 give samples that deviate greatly from the expected stoichiometry (because of their positive enthalpy and free energy of formation). Nevertheless, such materials do differ from the bulk 3D perovskite properties, and they lie at the broad interface between the finite n-size 2D perovskites, extended in this work to the n = 7 member, and n = ∞, where trace amounts of the spacer amine are capable of altering the bulk crystal morphology (33). Rather than 2D perovskites, these materials should perhaps be termed “quasi-2D perovskites,” marking the territory defined between the crystallographically ordered 2D layers (5 nm, n = 7) on the lower end and the quantum barrier on the higher end, estimated either from the experimentally observed crystallite size (~10 nm, “n = 15”) (34) or by the quantum confinement limit of colloidal nanocrystals (12 nm, “n = 18”) (35). These findings are in line with recent density functional theory (DFT) calculations on the thermodynamic stability of oxide perovskites, which predict that there is a certain limit in ΔG that serves to preclude the synthesis of higher n-members in pure form (36). Processes such as phase segregation, disproportionation, or composite material formation via intergrowth of various phases may be operating, as this has been confirmed experimentally in the growth of oxide perovskite films (37–39) and related oxides (40). The synthesis of higher n compounds may still be achievable using methods designed to exercise good kinetic control.

**Optical and Electronic Properties.** One of the most appealing features of 2D RP perovskites is the rational manner in which their optical properties [band gap (E<sub>g</sub>), exciton binding energy (E<sub>b</sub>), etc.] can be tuned as a function of n, allowing access to study their unique quasidimensional physics (33). This property derives from the inherent multiple QW-like structure, which arises from the ordered stacking of finite thickness perovskite layers alternating with organic spacers within a crystal grain, allowing for quantum properties to be obtained in a bulk material (Fig. 3 A and B). Thus far, the E<sub>g</sub> values from n = 1–5 have been reported (4), and the new n = 6 and n = 7 entries serve to bridge the

**Table 2. Selected structural and physical properties of the (BA)<sub>2</sub>(MA)<sub>n-1</sub>Pb<sub>n</sub>I<sub>3n+1</sub> perovskites**

Compound	n	A, Å	C, Å	B, Å	P, g/cm <sup>3</sup>	Pb–I–Pb angle min/max, °	PL emission, nm	Bandgap, eV	ΔH <sub>f</sub> , kJ/mol
BA <sub>2</sub> PbI <sub>4</sub> (50)	1	8.863 (2)	8.682 (1)	27.570 (2)	2.702	155.19 (6)	525	2.25	-49.69 ± 1.18
BA <sub>2</sub> MAPb <sub>2</sub> I <sub>7</sub>	2	8.947 (1)	8.859 (1)	39.347 (2)	3.159	164.3 (3)/173.1 (3)	580	1.97	-67.90 ± 1.47
BA <sub>2</sub> MA <sub>2</sub> Pb <sub>3</sub> I <sub>10</sub>	3	8.928 (1)	8.878 (1)	51.959 (4)	3.392	164.6 (2)/172.3 (2)	618	1.86	-28.74 ± 1.25
BA <sub>2</sub> MA <sub>3</sub> Pb <sub>4</sub> I <sub>13</sub>	4	8.927 (1)	8.882 (1)	64.383 (3)	3.543	162.6 (1)/172.9 (1)	652	1.75	-80.62 ± 3.12
BA <sub>2</sub> MA <sub>4</sub> Pb <sub>5</sub> I <sub>16</sub>	5	8.931 (1)	8.905 (1)	77.013 (4)	3.6252	164.7 (1)/171.6 (1)	678	1.66	-20.47 ± 2.11
BA <sub>2</sub> MA <sub>5</sub> Pb <sub>6</sub> I <sub>19</sub>	6	8.905 (1)	8.885 (1)	89.424 (9)	3.7203	161.4 (9)/173.3 (9)	698	1.59	138.59 ± 1.48
BA <sub>2</sub> MA <sub>6</sub> Pb <sub>7</sub> I <sub>22</sub>	7	8.913 (1)	8.900 (1)	101.959 (15)	3.7639	156.0 (1)/174.0 (3)	713	1.57	242.06 ± 1.97
MAPbI <sub>3</sub> (51)	∞	8.849 (2)	8.849 (2)	12.642 (2)	4.159	163.6 (1)/180	775	1.52	34.50 ± 1.01

ΔH<sub>f</sub>, enthalpy of formation (in kilojoules per mole).

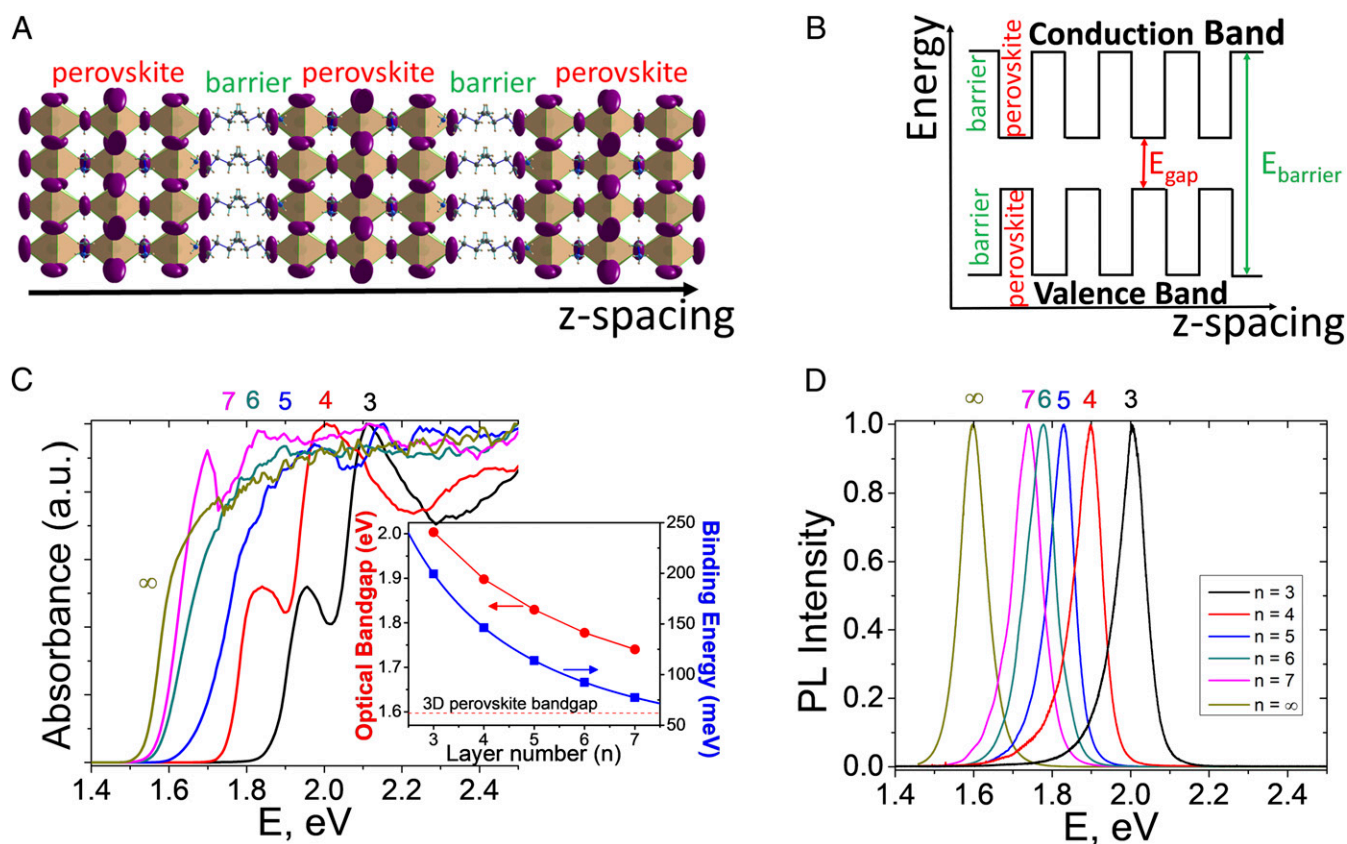


**Fig. 3.** Optical properties of 2D RP  $n = 3-7$ . (A) The structural configuration that defines the 2D perovskite multiple QW, which results in the characteristic energy diagram shown in B. (C) Optical gaps derived from the diffuse reflectance measurements of the  $(\text{BA})_2(\text{MA})_{n-1}\text{Pb}_n\text{I}_{3n+1}$  series ( $n = 3-7, \infty$ ). The *Inset* shows (red line) the optical bandgap as a function of  $n$  value derived from the photoluminescence (PL) spectra and (blue line) the corresponding expected exciton binding energy  $E_b$  calculated from the analytical model for 2D perovskites detailed in ref. 33 (refs. 4 and 41), illustrating a decrease in optical gap and PL emission energy with increasing  $n$ . (D) PL emission spectra of the  $(\text{BA})_2(\text{MA})_{n-1}\text{Pb}_n\text{I}_{3n+1}$  series ( $n = 3-7, \infty$ ).

chasm between the nanoscale and the bulk. The optical bandgap measured from absorption spectra (Fig. 3C) and photoluminescence (Fig. 3D) decreases monotonically with increasing  $n$  for  $n = 1-7$  RP perovskites due to change in the quantum and dielectric confinement effects, with  $E_g = 1.78$  eV for  $n = 6$  and  $E_g = 1.74$  eV for  $n = 7$ , respectively. The strong excitonic features typically observed in lower  $n$ -members are less pronounced in the  $n = 6$  and  $n = 7$  compounds, which was confirmed by the decrease of the calculated exciton binding energy to about 90 meV for  $n = 6$  and 75 meV for  $n = 7$  (41). The key physical properties of all structurally characterized 2D RP  $(\text{BA})_2(\text{MA})_{n-1}\text{Pb}_n\text{I}_{3n+1}$  perovskite phases are given in Table 2.

Electronically, the 2D halide perovskites are direct bandgap semiconductors at the  $\Gamma$ -point, showing a large band dispersion around the valence band maximum (VBM), consisting of hybridized, filled Pb-6s and I-5p orbitals, while the conduction band minimum (CBM) mainly consists of empty Pb-6p orbitals (Fig. 4A and B). A distinctive difference between 2D and 3D perovskites is that the originally degenerate bands deriving from the Pb-I bonding in  $\text{MAPbI}_3$  become split in the 2D perovskites revealing a number of finite subbands equal to the number of  $n$ -layers in the  $(\text{BA})_2(\text{MA})_{n-1}\text{Pb}_n\text{I}_{3n+1}$  formula, suggesting that each layer is electronically independent. As a consequence of this trend, both VBM and CBM are localized in a specific atomic domain within each individual perovskite slab, with CBM selectively preferring the  $[\text{PbI}_6]$  layers close to the spacer cations and VBM localizing in the central  $[\text{PbI}_6]$  layers, as shown for  $(\text{BA})_2(\text{MA})_6\text{Pb}_7\text{I}_{22}$  in Fig. 4C. The multiple QW nature of the 2D perovskites gives rise to dielectric confinement, arising from the

mismatch between the low dielectric constant organic spacers and high dielectric constant perovskite layers (31). As the inorganic layers become thicker, they dominate the dielectric properties of the material, asymptotically approaching the 3D perovskite (Fig. 4E).

**Thermal Stability and Temperature Evolution.** The homologous RP perovskites exhibit excellent thermal stability at temperatures below 600 K as shown by thermogravimetric analysis (TGA) (*SI Appendix, Fig. S2*). The decomposition temperature is marked by the dissociation of the organic ammonium salts (BA, MA) into the primary amine and hydrogen iodide, followed by a second step where molten  $\text{PbI}_2$  deiodinates to liquid Pb at  $\sim 750$  K. The pattern is similar for all RP members, with the notable difference that the two discrete decomposition temperature steps converge into a single step at  $\sim 650$  K for higher  $n$ -members.

The most interesting and technologically relevant part of the thermal behavior of the  $(\text{BA})_2(\text{MA})_{n-1}\text{Pb}_n\text{I}_{3n+1}$  perovskites is that the structural phase transitions close to and below room temperature. These changes can be probed by differential scanning calorimetry (DSC) in the 80–400 K range (Fig. 5A). RP perovskites exhibit two distinctive phase transitions reminiscent of those in  $\text{MAPbI}_3$ , which changes from the cubic  $\alpha$ -phase to the tetragonal  $\beta$ -phase below  $\sim 333$  K and from the tetragonal  $\beta$ -phase to the orthorhombic  $\gamma$ -phase below  $\sim 156$  K, in accord with previous reports (42–45). Zoomed-in views of the transition regions (in Fig. 5B) show a dependence of the transition temperature on  $n$  for the  $\beta$ - $\gamma$  transition, whereas the  $\alpha$ - $\beta$  transition is invariant with  $n$  (Fig. 5C). The double peaks for  $n = 6$  arise as a

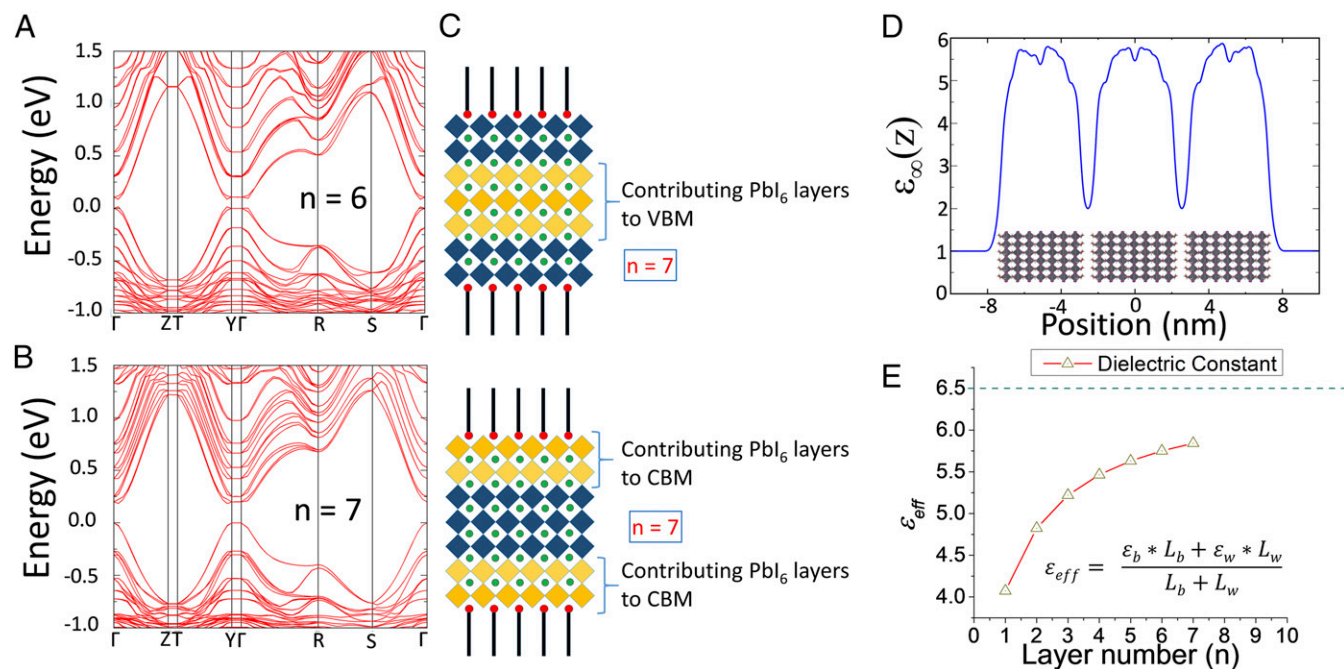


**Fig. 4.** Electronic structure and dielectric properties of 2D RP  $n = 6, 7$ . Calculated band structures of the (A)  $n = 6$  and (B)  $n = 7$  members of the  $(\text{BA})_2(\text{MA})_{n-1}\text{Pb}_n\text{I}_{3n+1}$  series. (C) Graphical representation of the main atomic contributions of the valence (VBM) and conduction (CBM) bands for  $(\text{BA})_2(\text{MA})_5\text{Pb}_7\text{I}_{22}$ , illustrating the localization of the wavefunction at the band extrema. A schematic is used here for clarity where the blue and yellow octahedra are meant to signify the main contributing atoms to the respective VB and CB extrema. The actual calculated  $\Gamma$  point wavefunctions are given in *SI Appendix, Fig. S6*. (D) The calculated high-frequency dielectric constant ( $\epsilon_\infty$ ) for  $(\text{BA})_2(\text{MA})_5\text{Pb}_7\text{I}_{22}$  along the stacking direction, with the structural model used in the *Inset*. (E) Graphical evolution of the effective high-frequency dielectric constant  $\epsilon_{\text{eff}}$  as a function of the layer number  $n$  based on the model proposed by Ishihara and coworkers (31) ( $L_b/L_w$ , length of barrier/well;  $\epsilon_b, \epsilon_w$ , dielectric constant of barrier/well;  $\epsilon_b$  is essentially independent of  $n$ ). The dashed line is the  $\epsilon_\infty$  value of  $\text{MAPbI}_3$  (49).

result of  $n = \infty$  second phase and manifest themselves in both regions. Corroborated by the in situ SXR analysis and following similar nomenclature, we call the orthorhombic phase above 283 K the  $\alpha$ -phase, the phase between 283 and 150–190 K (depending on  $n$ ) the  $\beta$ -phase, and the phase below 160 K (depending on  $n$ ) the  $\gamma$ -phase (Fig. 5D). All of these phases have the same 2D perovskite structure and involve subtle changes in the rotations of the Pb-based octahedra.

This classification of the 2D perovskites in a structural phase diagram is useful in probing the fundamental differences among 2D perovskites with different organic spacers, which can show drastic differences in their optoelectronic performance. For example, the main analog of the  $(\text{BA})_2(\text{MA})_{n-1}\text{Pb}_n\text{I}_{3n+1}$  family,  $(\text{PEA})_2(\text{MA})_{n-1}\text{Pb}_n\text{I}_{3n+1}$  (PEA stands for the phenylethylammonium cation), adopts the low-symmetry structure ( $\gamma$ -phase) at room temperature for all  $n$ -members (14, 22), yet it is able to produce some of the brightest perovskite light-emitting devices (LEDs) known to date (15). Understanding these subtle structure–property variations that produce such different electronic effects is of great importance in utilizing the 2D perovskites toward specific applications.

The nature of the two structural transitions in  $(\text{BA})_2(\text{MA})_{n-1}\text{Pb}_n\text{I}_{3n+1}$ , however, is different from that in  $\text{MAPbI}_3$ . The transition at 283–285 K does not vary with  $n$ , suggesting an exclusive dependence of the transition temperature with the nature of the organic spacers. In fact, this can be directly observed in SXR as a sharp contraction along the stacking axis evident by a shift of the  $(0k0)$  reflections to higher angles accompanied by an asymmetric stretching in the perovskite plane, evident by the increasing separation between the (200) and (002) reflections. The low temperature transition is strongly dependent on the inorganic framework thickness, decreasing with increasing  $n$ , and approximating the transition temperature of  $\text{MAPbI}_3$  for high  $n$ -members. The structural changes are minor, manifested by splitting of few reflections that suggest a structural change to a

triclinic structure, possibly reflecting the change from a dynamically disordered structure to an ordered one, by analogy to the 3D perovskites (46). The change in the transition temperature appears to vary with the effective electrostatic attraction between the  $[(\text{BA})_2]^{2+}$  bilayers and the  $[\text{MA}_{n-1}\text{Pb}_n\text{I}_{3n+1}]^{2-}$  inorganic layers, which decreases with increasing  $n$  (each layer is less neutral as the “2–” charge is distributed among more atoms).

**Thin Films and Device Fabrication: Implications for Photovoltaics.** In an initial attempt to understand how the thermodynamic stability of the perovskites influences the photovoltaic properties, we fabricated devices of the  $n = 6$  and  $n = 7$  RP perovskites. Following our previous studies we employed the hot-casting method (47), yielding compact, high-quality dark brown films with the average root-mean-square (rms) roughness of 26.5 and 19.4 nm, respectively (*SI Appendix, Fig. S7*), exhibiting good preferential orientation of the layers, normal to the devices’ substrate (*SI Appendix, Fig. S8*). In contrast to these  $n = 6$  and  $n = 7$  films, the hot-cast film of “ $n = 9$ ” actually had poor crystallinity. As illustrated in *SI Appendix, Fig. S9*, the stability of the  $n = 6$  and  $n = 7$  members is excellent, much superior to  $\text{MAPbI}_3$ , as shown by the stability tests that were conducted under ambient conditions at 30–40% relative humidity, as judged by the  $\text{PbI}_2$  degradation peak evolution. Lower- $n$  films appear to be more resistant to moisture than the higher  $n$ , as might be expected from their greater thermodynamic stability.

The solar cell device PCE of the  $n = 6$ ,  $n = 7$ , and “ $n = 9$ ” films, evaluated by assembling the hot-cast films into a simple planar heterojunction device structure, revealed a declining trend in device efficiency with  $\eta = 10.90\%$  and  $\eta = 8.93\%$  for the former two, respectively, and an enhancement for “ $n = 9$ ” to reach  $\eta = 12.63\%$  (Fig. 6A). External quantum efficiency supports this trend, suggesting that as  $n$  increases, so does the efficiency of the material to convert the absorbed photons at longer

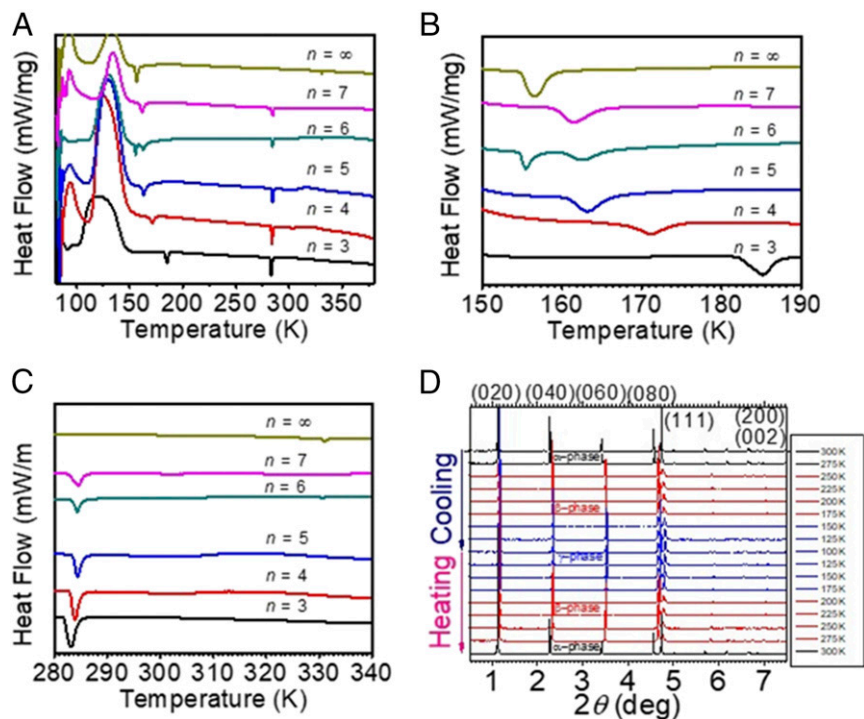


**Fig. 5.** Thermal stability of 2D RP  $n = 3$ –7. Temperature evolution of the 2D  $(\text{BA})_2(\text{MA})_{n-1}\text{Pb}_n\text{I}_{3n+1}$  ( $n = 3$ –7,  $\infty$ ) perovskite series. (A) DSC thermal profiles between 100 and 400 K revealing two sequential phase changes analogous to those in 3D perovskites. *B* and *C* represent zoomed-in views of the transition regions, illustrating a transition temperature dependence as a function of  $n$  for the  $\beta$ – $\gamma$  transition (*B*), whereas the  $\alpha$ – $\beta$  transition (*C*) is invariant with  $n$ . The double peak for  $n = 6$  arise as a result of  $n = \infty$  second phase and manifests themselves in both regions. The thermal events are confirmed by differential temperature synchrotron X-ray diffraction to be structural phase transitions, exemplified for  $n = 3$  in *D*, which are reversible and correspond to changes from the room temperature  $\alpha$ -phase to the low-temperature  $\gamma$ -phase below  $\sim 160$  K through the  $\beta$ -phase, which occurs just below room temperature.

wavelengths (Fig. 6*B*). Detailed photovoltaic parameters for these devices are listed in *SI Appendix, Table S11*. The typical  $J$ – $V$  curves under reverse and forward bias are shown in *SI Appendix, Fig. S10*.

Comparing the trends in thermodynamic stability discussed above (Fig. 2 *C* and *D*) and the champion device PCE of  $n = 3$ –7 and “ $n = 9$ ” (Fig. 6*A*), we observe a remarkable similarity; the thermodynamically favorable even-layered perovskites show a tendency toward higher device performance with respect to the less stable odd-layered perovskites. Despite the possibility that this connection is incidental, due to other device engineering factors determining the PCE, this emerging trend may be tentatively rationalized by considering the materials’ thermodynamics. Even though the PCE efficiency tends to decrease with increasing  $n$ , once  $n$  crosses the thermodynamic instability threshold of  $n = 7$ , PCE starts rising again, approaching the levels of the 3D perovskite. Although the rise in efficiency for “ $n = 9$ ” may arguably derive from the presence of  $\text{MAPbI}_3$  as an impurity phase, other contraindicating properties of the material, such as the distinct stacked-layer morphology of these crystals (Fig. 1) and the enhanced moisture stability of the respective films, suggest the presence of high- $n$  RP perovskites, either within the thermodynamic instability regime between  $n = 7$  and  $n = \infty$  (quasi-2D perovskites), or in the form of composite materials, similar to those observed recently in the 2D/3D  $(\text{HOOC}(\text{CH}_2)_4\text{NH}_3)_2\text{PbI}_4/\text{CH}_3\text{NH}_3\text{PbI}_3$  system (48).

## Conclusions

We have demonstrated the successful synthesis and crystal structures of  $n = 6$  and  $n = 7$ , which exhibit optical gaps of 1.78 and 1.74 eV, respectively. Our calorimetric measurements show a dramatic decrease in thermodynamic stability going from  $n = 5$  to  $n = 6$  and  $n = 7$ . The 2D perovskites with  $n > 5$  have a

positive enthalpy of formation ( $\Delta H_f$ ) with respect to binary compounds and  $\text{MAPbI}_3$ . Therefore, using the standard synthesis procedures, the ability to prepare single phase of higher- $n$  members is diminished with each increase of  $n$  beyond around  $n \sim 7$  as is the ability of X-ray diffraction to distinguish between the high  $n$ -members especially at  $n > \sim 8$ . We recommend the use of proton NMR ( $^1\text{H-NMR}$ ) as a tool for analysis to

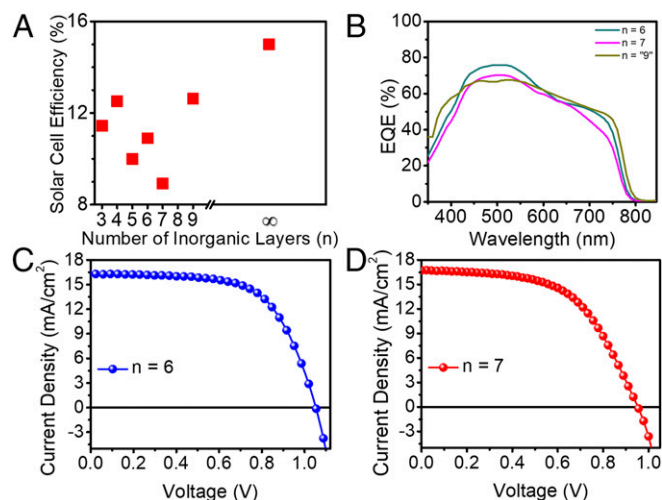


**Fig. 6.** Planar solar cells based on 2D RP  $n = 6, 7$ . (A) Planar solar cell efficiencies and of the  $(\text{BA})_2(\text{MA})_{n-1}\text{Pb}_n\text{I}_{3n+1}$  series as a function of the perovskite layer thickness ( $n$ ). (B) External quantum efficiencies for  $n = 6, 7$ , and “9.” Device  $J$ – $V$  curves are shown, (C)  $n = 6$  and (D)  $n = 7$ .

quantify the relative ratio between BA (or any other organic spacer cation) and MA (or any other cage cation) to derive chemical formulas. Nevertheless, positive enthalpies of formation do not preclude the synthesis of higher members; rather, we can use this information to design kinetically controlled routes to the compounds.

Thin films of higher  $n$  are highly crystalline and give compact and fully covered film morphologies. These films exhibit substantial improvement in moisture stability after long-term exposure to ambient air, with respect to the 3D MAPbI<sub>3</sub> films. Initial evaluation of photovoltaic performance of  $n = 6$  and  $n = 7$  shows very promising PCEs of 10.9% and 8.93%, respectively. The formation of mixtures of 2D perovskite phases, however, which may come in the form of perovskite intergrowths or composites could be a blessing from the point of view of optoelectronics, since these perovskite blends may combine the bright features of both the 2D and 3D perovskite or generate emergent properties.

## Methods

**Synthesis.** Perovskite crystals of (BA)<sub>2</sub>(MA)<sub>5</sub>Pb<sub>6</sub>I<sub>19</sub> and (BA)<sub>2</sub>(MA)<sub>6</sub>Pb<sub>7</sub>I<sub>22</sub> were synthesized by adopting the previously reported procedure (2), using one-half the required stoichiometry of  $n$ -butylamine (BA), targeting the hypothetical formula “(BA)(MA) <sub>$n-1$</sub> Pb <sub>$n+1$</sub> I <sub>$3n+1$</sub> ” and using larger quantities of starting material (SI Appendix, Table S12). PbO powder (4.464 g, 20 mmol) was dissolved in a mixture of aqueous HI solution (20.0 mL, 152 mmol) and aqueous H<sub>3</sub>PO<sub>2</sub> (3.4 mL, 31.0 mmol) by heating to boiling under constant magnetic stirring for 20 min, forming a bright yellow solution. Subsequent addition of solid MAI [1,125 mg, 16.67 mmol ( $n = 6$ ); 1,157 mg, 17.14 mmol ( $n = 7$ ); 1,200 mg, 17.78 mmol (“ $n = 9$ ”)] to the hot yellow solution initially causes precipitation of a black powder, which rapidly dissolves under stirring to afford a clear bright yellow solution. In a separate beaker, BA [331  $\mu$ L, 3.33 mmol ( $n = 6$ ); 283  $\mu$ L, 2.86 mmol ( $n = 7$ ); 220  $\mu$ L, 2.22 mmol (“ $n = 9$ ”)] was neutralized with HI (10 mL, 76 mmol) in an ice bath, resulting in a clear pale yellow solution. Addition of the chilled BA solution to the MAPbI<sub>3</sub> solution initially produces a black precipitate, which subsequently dissolves under heating the solution to boiling. The stirring is then discontinued, and the solution is allowed to cool to room temperature during which time black crystals begin to precipitate. After standing overnight, the crystals were isolated by suction filtration and thoroughly dried at 60 °C in a vacuum oven. All of the compounds discussed and characterized were prepared from

a single batch, so all of the relevant properties correspond to the exact same material.

**Isothermal Acid Solution Calorimetry.** A Calorimetry Sciences Corporation 4400 isothermal microcalorimeter operated at 25 °C was used for the measurements of enthalpy of dissolution. In a typical experiment, ~5 mg of each sample was hand-pressed into a pellet and dropped into 5 M HCl solvent (~25 g) equilibrated in the calorimetric sample chamber. Mechanical stirring was used to aid dissolution. The calorimeter was calibrated by dissolving 15-mg pellets of KCl in water with stirring at 25 °C.

**Supplementary Material.** Spectroscopic (IR, <sup>1</sup>H-NMR, TGA), crystallographic (crystallographic tables, calculated XRD patterns), and device fabrication and characterization (film stability, device cycling) information can be found in SI Appendix. The crystallographic tables and refinement files for the  $n = 6$  and  $n = 7$  are provided in .cif format.

**ACKNOWLEDGMENTS.** This work was supported by Office of Naval Research Grant N00014-17-1-2231 (synthesis and stability studies). The device fabrication part of this work was supported by Center for Light Energy Activated Redox Processes (LEAP), an Energy Frontier Research Center funded by the US Department of Energy, Office of Science, Office of Basic Energy Sciences, under Award DE-SC0001059. The work at Los Alamos National Laboratory (LANL) was supported by Department of Energy, Office of Basic Energy Sciences Award 08SPCE973, and by the LANL Laboratory Directed Research and Development Program. The work at Institut des Sciences Chimiques de Rennes was supported by Agence Nationale pour la Recherche (TRANSHYPERO Project) and was granted access to the high-performance computing resources of Très Grand Centre de Calcul/Centre Informatique National de l'Enseignement Supérieur/ Institut du Développement et des Ressources en Informatique Scientifique under the allocation 2017-A0010907682 made by Grand Equipement National de Calcul Intensif. J.E. acknowledges support by Institut Universitaire de France. The calorimetric work at University of California, Davis, was supported by US Department of Energy Grant DE-FG02-03ER46053. Electron microscopy was performed at the Electron Probe Instrumentation Center at Northwestern University. Confocal microscopy studies were performed at the Scanned Probe Imaging and Development Facility [Northwestern University's Atomic and Nanoscale Characterization Experimental Center (NUANCE) Center]. The NUANCE Center is supported by the International Institute for Nanotechnology, Materials Research Science and Engineering Center (National Science Foundation Grant DMR-1121262), the Keck Foundation, the State of Illinois, and Northwestern University. Use of the Advanced Photon Source at Argonne National Laboratory was supported by the US Department of Energy, Office of Science, Office of Basic Energy Sciences, under Contract DE-AC02-06CH11357.

- Stoumpos CC, et al. (2017) High members of the 2D Ruddlesden–Popper halide perovskites: Synthesis, optical properties, and solar cells of (CH<sub>3</sub>(CH<sub>2</sub>)<sub>3</sub>NH<sub>3</sub>)<sub>2</sub>(CH<sub>3</sub>NH<sub>3</sub>)<sub>4</sub>Pb<sub>5</sub>I<sub>16</sub>. *Chem* 2:427–440.
- Stoumpos CC, et al. (2016) Ruddlesden–Popper hybrid lead iodide perovskite 2D homologous semiconductors. *Chem Mater* 28:2852–2867.
- Tsai H, et al. (2016) High-efficiency two-dimensional Ruddlesden–Popper perovskite solar cells. *Nature* 536:312–316.
- Blanco J-C, et al. (2017) Extremely efficient internal exciton dissociation through edge states in layered 2D perovskites. *Science* 355:1288–1292.
- Cao DH, Stoumpos CC, Farha OK, Hupp JT, Kanatzidis MG (2015) 2D homologous perovskites as light-absorbing materials for solar cell applications. *J Am Chem Soc* 137:7843–7850.
- Mao L, et al. (2016) Role of organic counterion in lead- and tin-based two-dimensional semiconducting iodide perovskites and application in planar solar cells. *Chem Mater* 28:7781–7792.
- Mao L, Wu Y, Stoumpos CC, Wasielewski MR, Kanatzidis MG (2017) White-light emission and structural distortion in new corrugated 2D lead bromide perovskites. *J Am Chem Soc* 139:5210–5215.
- Mitzi DB, Wang S, Feild CA, Chess CA, Guloy AM (1995) Conducting layered organic-inorganic halides containing <110>-oriented perovskite sheets. *Science* 267:1473–1476.
- Mitzi DB, Feild CA, Harrison WTA, Guloy AM (1994) Conducting tin halides with a layered organic-based perovskite structure. *Nature* 369:467–469.
- Kagan CR, Mitzi DB, Dimitrakopoulos CD (1999) Organic-inorganic hybrid materials as semiconducting channels in thin-film field-effect transistors. *Science* 286:945–947.
- Saparov B, Mitzi DB (2016) Organic-inorganic perovskites: Structural versatility for functional materials design. *Chem Rev* 116:4558–4596.
- Mitzi DB (2001) Templating and structural engineering in organic-inorganic perovskites. *J Chem Soc Dalton Trans*, 1–12.
- Smith MD, et al. (2017) Decreasing the electronic confinement in layered perovskites through intercalation. *Chem Sci (Camb)* 8:1960–1968.
- Smith IC, Hoke ET, Soles-Ibarra D, McGehee MD, Karunadasa HI (2014) A layered hybrid perovskite solar-cell absorber with enhanced moisture stability. *Angew Chem Int Ed Engl* 53:11232–11235.
- Yuan M, et al. (2016) Perovskite energy funnels for efficient light-emitting diodes. *Nat Nanotechnol* 11:872–877.
- Sapori D, Kepenekian M, Pedesseau L, Katan C, Even J (2016) Quantum confinement and dielectric profiles of colloidal nanoplatelets of halide inorganic and hybrid organic-inorganic perovskites. *Nanoscale* 8:6369–6378.
- Even J, Pedesseau L, Katan C (2014) Understanding quantum confinement of charge carriers in layered 2D hybrid perovskites. *ChemPhysChem* 15:3733–3741.
- Pedesseau L, et al. (2016) Advances and promises of layered halide hybrid perovskite semiconductors. *ACS Nano* 10:9776–9786.
- Quan LN, et al. (2016) Ligand-stabilized reduced-dimensionality perovskites. *J Am Chem Soc* 138:2649–2655.
- Ishihara T, Takahashi J, Goto T (1989) Exciton state in two-dimensional perovskite semiconductor (C<sub>10</sub>H<sub>21</sub>NH<sub>3</sub>)<sub>2</sub>PbI<sub>4</sub>. *Solid State Commun* 69:933–936.
- Shibuya K, Koshimizu M, Takeoka Y, Asai K (2002) Scintillation properties of (C<sub>6</sub>H<sub>13</sub>NH<sub>3</sub>)<sub>2</sub>PbI<sub>4</sub>: Exciton luminescence of an organic/inorganic multiple quantum well structure compound induced by 2.0 MeV protons. *Nucl Instrum Methods Phys Res B* 194:207–212.
- Calabrese J, et al. (1991) Preparation and characterization of layered lead halide compounds. *J Am Chem Soc* 113:2328–2330.
- Soe CMM, et al. (2017) New type of 2D perovskites with alternating cations in the interlayer space, (C(NH<sub>2</sub>)<sub>2</sub>)<sub>3</sub>(CH<sub>3</sub>NH<sub>3</sub>) <sub>$n$</sub> Pb <sub>$n+1$</sub> I <sub>$3n+1$</sub> : Structure, properties, and photovoltaic performance. *J Am Chem Soc* 139:16297–16309.
- Mao L, et al. (2017) Tunable white-light emission in single-cation-templated three-layered 2D perovskites (CH<sub>3</sub>CH<sub>2</sub>NH<sub>3</sub>)<sub>4</sub>Pb<sub>3</sub>Br<sub>10-x</sub>Cl <sub>$x$</sub> . *J Am Chem Soc* 139:11956–11963.
- Mao L, et al. (2018) Hybrid Dion–Jacobson 2D lead iodide perovskites. *J Am Chem Soc* 140:3775–3783.
- Soe CMM, et al. (2018) Understanding film formation morphology and orientation in high member 2D Ruddlesden–Popper perovskites for high-efficiency solar cells. *Adv Energy Mater* 8:1700979.
- Tanaka K, et al. (2005) Image charge effect on two-dimensional excitons in an inorganic-organic quantum-well crystal. *Phys Rev B Condens Matter Mater Phys* 71:045312.

8 of 9 | www.pnas.org/cgi/doi/10.1073/pnas.1811006115

Soe et al.

28. Papavassiliou GC, Koutselas IB (1995) Structural, optical and related properties of some natural three- and lower-dimensional semiconductor systems. *Synth Met* 71: 1713–1714.
29. Koutselas IB, Ducasse L, Papavassiliou GC (1996) Electronic properties of three- and low-dimensional semiconducting materials with Pb halide and Sn halide units. *J Phys Condens Matter* 8:1217–1227.
30. Yaffe O, et al. (2015) Excitons in ultrathin organic-inorganic perovskite crystals. *Phys Rev B Condens Matter Mater Phys* 92:045414.
31. Hong X, Ishihara T, Nurmikko AV (1992) Dielectric confinement effect on excitons in  $\text{PbI}_2$ -based layered semiconductors. *Phys Rev B Condens Matter* 45:6961–6964.
32. Nagabhushana GP, Shivaramaiah R, Navrotsky A (2016) Direct calorimetric verification of thermodynamic instability of lead halide hybrid perovskites. *Proc Natl Acad Sci USA* 113:7717–7721.
33. Jao M-H, Lu C-F, Tai P-Y, Su W-F (2017) Precise facet engineering of perovskite single crystals by ligand-mediated strategy. *Cryst Growth Des* 17:5945–5952.
34. Xiao Z, et al. (2017) Efficient perovskite light-emitting diodes featuring nanometre-sized crystallites. *Nat Photonics* 11:108–115.
35. Protesescu L, et al. (2015) Nanocrystals of cesium lead halide perovskites ( $\text{CsPbX}_3$ , X = Cl, Br, and I): Novel optoelectronic materials showing bright emission with wide color gamut. *Nano Lett* 15:3692–3696.
36. Glasser L (2017) Systematic thermodynamics of layered perovskites: Ruddlesden-Popper phases. *Inorg Chem* 56:8920–8925.
37. Lee C-H, et al. (2013) Effect of reduced dimensionality on the optical band gap of  $\text{SrTiO}_3$ . *Appl Phys Lett* 102:122901.
38. Yan L, et al. (2011) Cation ordering within the perovskite block of a six-layer Ruddlesden-Popper oxide from layer-by-layer growth—artificial interfaces in complex unit cells. *Chem Sci* 2:261–272.
39. Lee C-H, et al. (2013) Exploiting dimensionality and defect mitigation to create tunable microwave dielectrics. *Nature* 502:532–536.
40. Anderson JS, et al. (1973) Point defects and extended defects in niobium oxides. *Nature* 243:81–83.
41. Blancon JC, et al. (2018) Scaling law for excitons in 2D perovskite quantum wells. *Nat Commun* 9:2254.
42. Soe CMM, et al. (2016) Room temperature phase transition in methylammonium lead iodide perovskite thin films induced by hydrohalic acid additives. *ChemSusChem* 9: 2656–2665.
43. Onoda-Yamamuro N, Matsuo T, Suga H (1990) Calorimetric and IR spectroscopic studies of phase transitions in methylammonium trihalogenoplumbates (II). *J Phys Chem Solids* 51:1383–1395.
44. Baikie T, et al. (2013) Synthesis and crystal chemistry of the hybrid perovskite  $(\text{CH}_3\text{NH}_3)\text{PbI}_3$  for solid-state sensitised solar cell applications. *J Mater Chem A* 1: 5628–5641.
45. Knop O, et al. (1990) Alkylammonium lead halides. Part 2.  $\text{CH}_3\text{NH}_3\text{PbX}_3$  (X=Cl, Br, I) perovskites: Cuboctahedral halide cages with isotropic cation reorientation. *Can J Chem* 68:412–422.
46. Yaffe O, et al. (2017) Local polar fluctuations in lead halide perovskite crystals. *Phys Rev Lett* 118:136001.
47. Nie W, et al. (2015) Solar cells. High-efficiency solution-processed perovskite solar cells with millimeter-scale grains. *Science* 347:522–525.
48. Grancini G, et al. (2017) One-year stable perovskite solar cells by 2D/3D interface engineering. *Nat Commun* 8:15684.
49. Hirasawa M, Ishihara T, Goto T, Uchida K, Miura N (1994) Magnetoabsorption of the lowest exciton in perovskite-type compound  $(\text{CH}_3\text{NH}_3)\text{PbI}_3$ . *Physica B* 201: 427–430.
50. Mitzi DB (1996) Synthesis, crystal structure, and optical and thermal properties of  $(\text{C}_4\text{H}_9\text{NH}_3)_2\text{MI}_4$  (M = Ge, Sn, Pb). *Chem Mater* 8:791–800.
51. Stoumpos CC, Malliakas CD, Kanatzidis MG (2013) Semiconducting tin and lead iodide perovskites with organic cations: Phase transitions, high mobilities, and near-infrared photoluminescent properties. *Inorg Chem* 52:9019–9038.